The Astrophysical Journal Letters, 911:L4 (14pp), 2021 April 10 https://doi.org/10.3847/2041-8213/abe775

Identifying the Coronal Source Regions of Solar Wind Streams from Total Solar Eclipse Observations and in situ Measurements Extending over a Solar Cycle

Shadia R. Habbal[1], Miloslav Druckmüller[2], Nathalia Alzate[3], Adalbert Ding[4], Judd Johnson[5], Pavel Starha[2], Jana Hoderova[2], Benjamin Boe[1], Sage Constantinou[1], and Martina Arndt[6]
[1] Institute for Astronomy, University of Hawaii, 2680 Woodlawn Drive, Honolulu, HI, USA; shadia@ifa.hawaii.edu
[2] Faculty of Mechanical Engineering, Brno University of Technology, 616 69 Brno, Czech Republic
[3] NASA, Goddard Space Flight Center, Heliophysics Science Division, Greenbelt, MD, and Universities Space Research Association (USRA), Columbia, MD, USA
[4] Institute of Optics and Atomic Physics, Technische Universität, and Institute for Technical Physics, Berlin, Germany
[5] Electricon, Boulder, CO, USA
[6] Bridgewater State University, Bridgewater, MA, USA
Received 2020 December 30; revised 2021 February 11; accepted 2021 February 18; published 2021 April 12

Abstract

This letter capitalizes on a unique set of total solar eclipse observations acquired between 2006 and 2020 in white light, Fe XI 789.2 nm ($T_{\rm fexi} = 1.2 \pm 0.1$ MK), and Fe XIV 530.3 nm ($T_{\rm fexiv} = 1.8 \pm 0.1$ MK) emission complemented by in situ Fe charge state and proton speed measurements from Advanced Composition Explorer/SWEPAM-SWICS to identify the source regions of different solar wind streams. The eclipse observations reveal the ubiquity of open structures invariably associated with Fe XI emission from Fe^{10+} and hence a constant electron temperature, $T_c = T_{\rm fexi}$, in the expanding corona. The in situ Fe charge states are found to cluster around Fe^{10+}, independently of the 300–700 km s^{-1} stream speeds, referred to as the continual solar wind. Thus, Fe^{10+} yields the fiducial link between the continual solar wind and its $T_{\rm fexi}$ sources at the Sun. While the spatial distribution of Fe XIV emission from Fe^{13+} associated with streamers changes throughout the solar cycle, the sporadic appearance of charge states $>Fe^{11+}$ in situ exhibits no cycle dependence regardless of speed. These latter streams are conjectured to be released from hot coronal plasmas at temperatures $\geqslant T_{\rm fexiv}$ within the bulge of streamers and from active regions, driven by the dynamic behavior of prominences magnetically linked to them. The discovery of continual streams of slow, intermediate, and fast solar wind characterized by the same $T_{\rm fexi}$ in the expanding corona places new constraints on the physical processes shaping the solar wind.

Unified Astronomy Thesaurus concepts: Solar prominences (1519); Solar cycle (1487); Solar wind (1534); Total eclipses (1704); Solar coronal streamers (1486); Solar magnetic fields (1503); Solar coronal heating (1989); Solar coronal mass ejections (310); Solar corona (1483)

1. Introduction

To identify the sources of different solar wind streams at the Sun, the topology of expanding coronal structures, as well as the link between their plasma parameters and corresponding in situ values, need to be established. To that end, the scientific value of simultaneous white light and multiwavelength observations of emission from forbidden line transitions in the corona acquired during total solar eclipses cannot be overstated. These observations remain unique as they capture ubiquitous open structures and their physical properties over a distance range of several solar radii (R_s), defined here as the expanding corona, a distance range currently beyond the reach of existing ground- and/or space-based instrumentation. The radial span of this emission is a consequence of the dominance of resonant over collisional excitation for these forbidden lines (see Habbal et al. 2007, 2013). It is within this radial span that a clear separation is established between the plasma that streams freely into interplanetary space, forming the solar wind, and the plasma that remains bound to the Sun, such as in active regions and loop-like structures, seemingly stacked with increasing heights, defining the bulges of streamers.

Furthermore, coronal emission from the Fe sequence in the visible and near-infrared, namely Fe IX to Fe XIV, provides a direct inference of the spatial distribution of the electron temperature in the corona (see Habbal et al. 2010a, 2011; Boe et al. 2020a) and hence places constraints on processes responsible for coronal heating and solar wind acceleration. This emission establishes a valuable link between the sources of the emitting Fe ions in the corona and their distribution in interplanetary space. The choice of Fe as an underlying common parameter to link the corona to the solar wind is obvious; it is the most abundant heavy element in the Sun, which can be easily observed both through the various forbidden emission lines in the corona and in situ via charge state measurements.

Sýkora (1992a, 1992b) was one of the first to draw attention to the potential connection between Fe XIV emission and the observed variability of the solar wind from ground-based coronagraphic Fe XIV observations spanning more than four solar cycles (SCs; see also Rušin & Rybansky 2002; Altrock 2004; Badalyan et al. 2005). The first study to quantitatively connect multiwavelength eclipse observations with in situ measurements was presented by Habbal et al. (2010b). Using observations from two eclipses, namely 2006 and 2008, and Advanced Composition Explorer (ACE) Solar Wind Ion Composition Spectrometer (SWICS) Fe charge state measurements (Gloeckler et al. 1998) from 1998 to 2009, these authors discovered the persistent presence of a narrow Fe charge state distribution centered around Fe^{10+}, directly linked

Table 1
Eclipse Dates with Corresponding Observing Sites, Observers, Carrington Rotation (CR) and Sunspot Cycle (SC)

ECLIPSE DATE	TIME (UT)	OBSERVING SITES & OBSERVERS	CR/**SC**
2006 March 29	10:13:57–10:18:03	Southern Sahara, Libya (Habbal & Co.)	2041/**23**
2008 August 1	11:03:35–11:05:39 11:13:17–11:15:06	Bor Uzur, Gobi Desert, Western Mongolia (Druckmüller & Co.) AlShan, Gobi Desert, Western China (Habbal & Co.)	2072
2009 July 7	03:28:39–03:34:20	Enewetak, Marshall Islands (Habbal & Co.)	2085
2010 July 11	18:45:36–18:50:05	Tatakoto, French Polynesia (Habbal & Co.)	2098/**24**
2012 November 13*	20:37:41–20:39:41	Queensland, Australia (David Finlay & Constantinos Emmanoulidis)	2130
2013 November 3*	13:52:40–13:53:45	Lamberene, Gabon (Constantinos Emmanoulidis)	2143
2015 March 20++	10:10:40–10:13:08	Longyearbyen, Svalbard (Habbal & Co.)	2161
2016 March 9*	00:22:11–00:24:03	Penyak Beach, Banka Island, Indonesia (Don Sabers, Ron Royer)	2176
2017 August 21++	17:21:11–17:23:14	Mitchell, Oregon (Habbal & Co.)	2194
2019 July 2++	20:40:03–20:42:16	Rodeo, Argentina (Habbal & Co.)	2219
2020 December 14*	16:07:59–16:10:04 16:21:11–16:23:20	Fortin Nogueira, Neuquen, Argentina (Andreas Möller) Bahia Creek, Rio Negro, Argentina (Dario Harari)	2238/**25**

to Fe XI emission in the corona, throughout SC 23. Lepri et al. (2001) also reported that the average Fe charge state in the ACE data from 1998 to 2000 ranged between Fe^{9+} and Fe^{11+}, and that the appearance of much higher charge states was associated with interplanetary coronal mass ejections (ICMEs). More recently, Stakhiv et al. (2016) analyzed ACE charge state measurements from 2007 to 2008 around solar minimum to search for signatures of the sources of the solar wind. They found that the slow wind has two components, one with properties very similar to the fast steady wind and another more variable wind. However, Lepri et al. (2001) and Stakhiv et al. (2016) did not have the coronal observations to link their in situ data back to the Sun.

This Letter capitalizes on the availability of a complement of contemporaneous coronal and in situ observations to identify the sources of the solar wind and the impact of solar activity on them. The coronal observations consist of a unique set of simultaneous white light, Fe XI, and Fe XIV total solar eclipse observations acquired between 2006 and 2020 from the descending phase of SC 23 to the beginning of SC 25. These data are complemented by in situ Fe charge state and solar wind speed measurements from ACE covering the same time period. We show how this complementary set of observations covering 14 years yields a link between the prevalence of Fe XI emission from Fe^{10+}, characterized by $T_{\rm fexi} = 1.2 \pm 0.1$ MK, in the expanding corona and the in situ presence of continual solar wind streams clustering around Fe^{10+} with speeds ranging from ≈300 to 700 km s^{-1}. These observations also suggest that the sporadic appearance of high Fe charge states in situ can be attributed to the dynamics of prominences at the base of streamers driving CMEs, as well as the more variable solar wind streams.

2. The Data: Total Solar Eclipse Observations and in situ Measurements between 2006 and 2020

2.1. High-resolution White Light and Multiwavelength Total Solar Eclipse Observations

Details of the total solar eclipse observations in white light and Fe coronal emission lines acquired between 2006 and 2020 are given in chronological order in Table 1, together with the corresponding Carrington rotation (CR) and SC numbers. In Figure 1, these observations are placed in the context of the monthly sunspot number with the dates of the eclipse observations given by colored circles. These observations straddle three cycles and coincide with different phases of solar activity. The 2006 eclipse occurred during the descending phase of SC 23, with its minimum at 2009. The SC 24 had two peaks in 2012 and 2013. The 2019 eclipse observations were acquired shortly before the minimum of SC 24 in December 2019. The 14 December 2020 eclipse was acquired at the beginning of SC 25. Since we were clouded out during the 2012, 2013, 2016, and 2020 eclipses, we used white light observations available from amateurs for those years. Unfortunately, since no other teams acquired multiwavelength observations comparable to ours, such observations are missing from these years.

High-resolution white light images were taken with commercially available large-format digital cameras, such as Nikon and Canon, outfitted with different focal length lenses using a sequence of exposure times. These images were processed by M. Druckmüller, who developed mathematical methods for the precise registration of images and the visualization of coronal structures using adaptive filters inspired by human vision (see Druckmüller 2009, 2013; Druckmüller et al. 2006).

Details of the instrumentation used for the multiwavelength Fe emission line observations and the data analysis techniques can be found in several publications (e.g., Habbal et al. 2011; Boe et al. 2020a). To summarize, observations for each coronal emission line are acquired with a pair of optical systems outfitted with 0.5 nm narrow bandpass filters. One unit in the pair is centered at the wavelength of the spectral line, and the other is 1–3 nm to the blue. This choice is dictated by the fact that spectral line intensities are only several percent of the intensity of the continuum in the 1–3 R_s distance range. To isolate the spectral line emission, the pair is operated simultaneously with the same sequence of exposure times. The data are corrected for dark and flat-field exposures

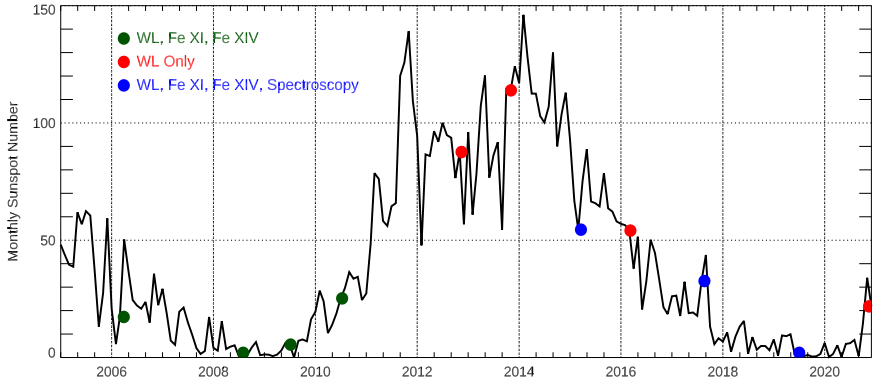

Figure 1. Plot of the monthly sunspot numbers with the dates of the eclipse observations given in Table 1, shown as colored circles. Green circles refer to dates with white light, Fe XI, and Fe XIV observations; red is for observations with white light only; and blue is the same as green with the addition of spectroscopy.

acquired after totality. They are then subtracted from each other. As a bonus, observations of the continuum at multiple wavelengths also yield scientifically valuable data pertaining to the properties of the F and K corona, as recently presented by Boe et al. (2021).

2.2. The in situ ACE data

To connect coronal structures to different solar wind streams, we complement the eclipse observations with the most comprehensive Fe charge state in situ data from 2006 to the end of 2020. These are available from the Solar Wind Electron, Proton, and Alpha Monitor (SWEPAM; McComas et al. 1998) and SWICS (Gloeckler et al. 1998) instruments on board the ACE spacecraft (Stone et al. 1998), which orbits around the Sun–Earth L1 Lagrangian point (see http://www.srl.caltech.edu/ACE/ASC/index.html). For the purpose of this study, we use the solar wind bulk velocities from ACE/SWEPAM and the Fe charge states from SWEPAM-SWICS, available in 12 minute averages. The ACE/SWICS data are available in two data sets corresponding to two different instruments, SWICS 1.1 and SWICS 2.0. The convenience of using this data set is that gaps in the SWEPAM data are filled with SWICS data, when available. An alteration in the instrument's operational state due to radiation and age resulted in the data gap between 2012 and 2013.

3. The Case for Fe XI and Fe XIV

The first total solar eclipse observation to include simultaneous continuum and multiwavelength imaging with narrow bandpass filters for the Fe X 637.4 nm and Fe XIV 530.3 nm lines was acquired by the Slovak expedition led by J. Sýkora to Siberia in 1981, very close to solar maximum. Shown in Figure 2(a), this composite image captures the clear distinction between emission from two spectral lines with different thermal properties. (As an aside, we note that this distinction was first reported by Mitchell 1932, albeit without his knowledge of the ions associated with these two wavelengths at that time.)

The distinction between the thermal properties of coronal forbidden lines is best demonstrated by the temperature dependence of the ionization fraction of the suite of Fe IX to Fe XIV lines in the visible to the near-infrared. Shown in Figure 2(b), the curves are calculated using data from Arnaud & Raymond (1992) with no assumption of collisional effects (see Boe et al. 2020a). These calculations yield peak ionization temperatures of ≈0.7, 1.0, 1.2, 1.7, and 1.8 MK, respectively. Their precise values can differ slightly from calculations using the more recent CHIANTI database (Dere et al. 2019), which yield 0.76, 1.05, 1.29, 1.74, and 1.95 MK, respectively (Landi, private communication). Consequently, we assume an uncertainty of 0.1 MK for these values in this work.

The curves in Figure 2(b) demonstrate that (1) over the 0.5–3 $\times$ 10^6 K range, different temperature plasmas can be readily targeted with observations in this sequence of Fe lines, and (2) there exist line pairs that enable the clear distinction between different temperature structures, such as Fe XI and Fe XIV. The first Fe XI 789.2 nm image of the corona, shown in red in the right panel of Figure 2(c) (cyan is from Fe XIII), was acquired during the 2006 March 29 total solar eclipse (Habbal et al. 2007, 2013). The unexpected spatial extent of the Fe XI emission led to the realization that emission from coronal forbidden lines is dominated by radiative excitation once collisional excitation diminishes significantly close to the Sun (Habbal et al. 2007, 2013). With a dependence of the emission on the ion number density and not the density squared, characteristic of collisionally excited extreme ultraviolet lines, emission from coronal forbidden lines can thus be detected out to much larger distances from the Sun.

The first simultaneous observations of the full Fe suite of Fe IX, Fe X, Fe XI, Fe XIII, and Fe XIV were acquired by Habbal et al. (2011) during the total solar eclipse of 2010 July 11. An image in Ni XV with a peak at 2.5 MK was also taken at that time to expand the temperature coverage, since Fe XV at 705.86 nm would be contaminated by a telluric absorption line. These observations showed that Fe IX emission was extremely weak, while Ni XV emission, which was limited to the bulges of streamers and active regions, was structureless compared to Fe XIV emission. They thus demonstrated that the best candidates for investigating the thermal properties of the corona are Fe X, Fe XI, Fe XIII, and Fe XIV.

It is clear from Figure 2(b) that imaging in either Fe X or Fe XI can be used to map the spatial distribution of the "cold" (≈1 MK) coronal structures. However, the higher abundance of Fe^{10+} (i.e., Fe XI emission) in the corona (see Habbal et al. 2010b) compared to Fe^{9+} (i.e., Fe X emission) favors the use of Fe XI. Further supporting evidence for the choice of Fe XI over Fe X is provided by the 2019 July 2 total solar eclipse observations shown in Figure 3, where the spatial extent of Fe XI emission exceeds that of Fe X. The comparison between Fe X and Fe XI in this figure further points to the fact that despite the proximity of their peak ionization temperatures, there are differences in coronal structure between these two lines. This implies that the thermal properties of coronal structures are distinguishable to within <0.2 MK.

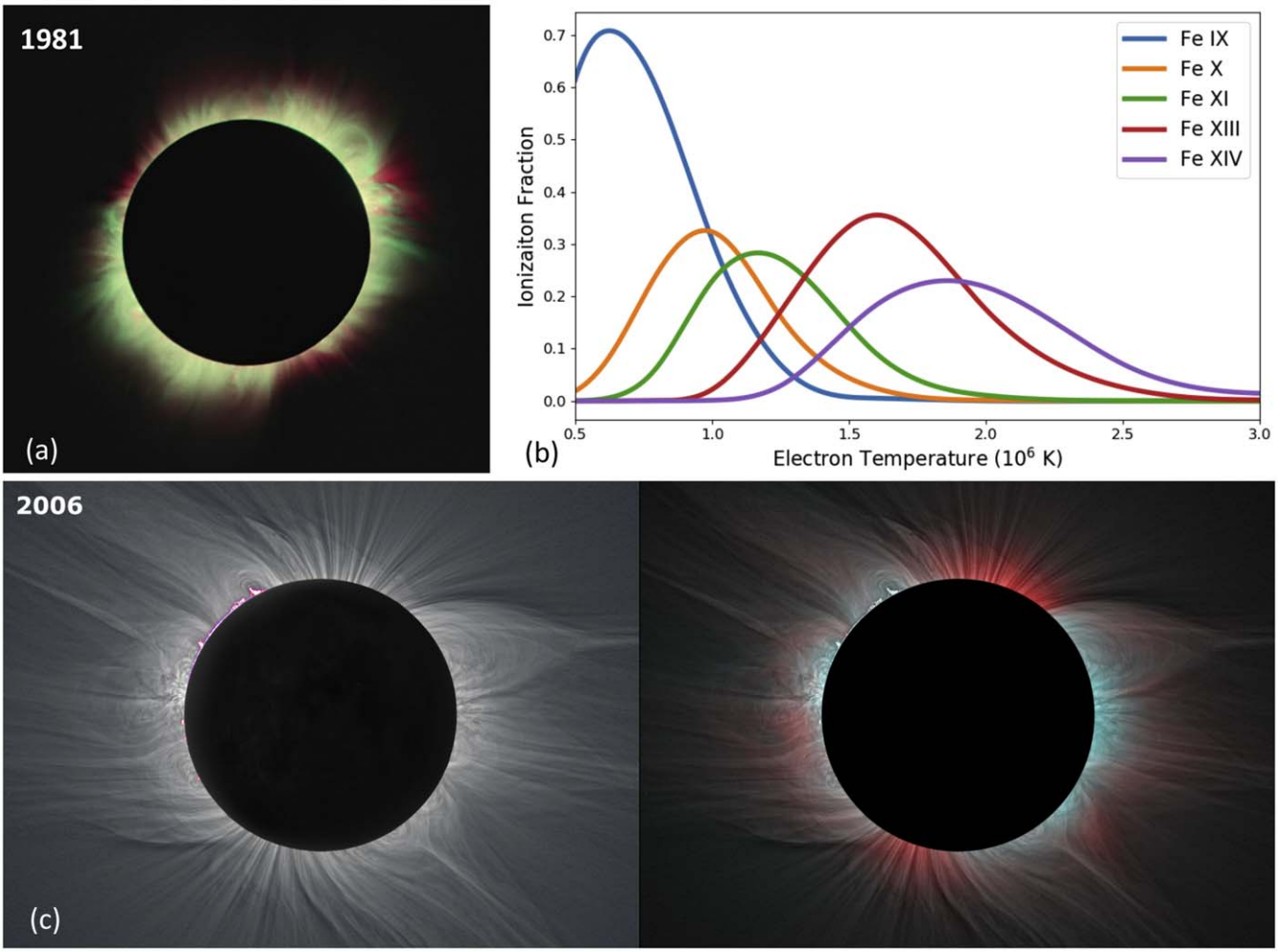

Figure 2. (a) Composite image of emission in continuum, Fe X 637.4 nm (red) with a 0.3 nm bandpass filter and Fe XIV 530.3 nm (green) with a 0.2 nm bandpass filter, from the 1981 eclipse taken with a 130/1950 mm refractor and recorded on black-and-white high-speed, high dynamic range Fomapan N800 film. The image was constructed and processed by M. Druckmüller. (b) Ionization fraction curves for the dominant coronal forbidden spectral lines and corresponding charge states (Boe et al. 2018), namely, Fe IX (Fe^{8+}), Fe X (Fe^{9+}), Fe XI (Fe^{10+}), Fe XIII (Fe^{12+}), and Fe XIV (Fe^{13+}). Note that Fe XII is absent in this sequence because its two emission lines at 303.3 and 356.1 nm are in the near-UV, which makes them more challenging to observe from the ground. (c) Eclipse composite image from the 2006 March 29 eclipse, with white light given in the left panel and a composite of white light, Fe XI (red), and Fe XIII 1074.7 nm (cyan) on the right.

For the hotter coronal structures, either Fe XIII or Fe XIV can be used to map the "hot" (≈2 MK) structures. However, Fe XIV is the clear winner for two reasons. (1) The continuum solar disk intensity at 530 nm is approximately three times stronger than that at 1074 nm. Hence, the radiative excitation of these two lines from the solar disk radiation enables the coronal structures in Fe XIV to be visible to much larger distances than for Fe XIII. (2) Standard CCD and CMOS cameras, such as the ones we use, have a very low quantum efficiency of ≈2%–5% at 1000 nm. This choice is further corroborated by the example of Figure 3, as it demonstrates why Fe XIV, whose spatial extent is significantly larger than that of Fe XIII, is a much better choice.

It thus becomes clear that Fe XI and Fe XIV emission, with their distinct temperature characteristics, remain the strongest among the Fe line sequence, thus dictating the choice of these two emission lines for the work presented here. Furthermore, given the clear distinction with their neighboring lines, i.e., Fe X for Fe XI and Fe XIII for Fe XIV, we argue that Fe XI and Fe XIV represent two relatively narrow temperature ranges, namely, $T_{\rm fexi} = 1.2 \pm 0.1$ and $T_{\rm fexiv} = 1.8 \pm 0.1$ MK, respectively.

4. Changes in the Spatial Distribution of Open Fine-scale Structures and the Electron Temperature

All Fe XI and Fe XIV total solar eclipse observations acquired simultaneously with 0.5 nm narrow bandpass filters are shown in Figures 2(c), 4, and 5. The layout in these figures is such that white light is given in the left panels and the Fe XI (red) and Fe XIV (green) composites, together with white light, are shown in the right panels (except in Figure 2(c), where Fe XIII in cyan replaces Fe XIV). Although both panels show the same field of view, we note that white light can be visible out to at least 15–20 R_s during eclipses, while the signal-to-noise ratio for the Fe XI and Fe XIV intensities becomes too weak to detect beyond 3 R_s. While white light visualizes all coronal structures independently of their temperature, a comprehensive visual representation of the thermal structure of coronal magnetic fields emerges when white light is combined with the distribution of Fe XI and Fe XIV emission, as is evident in the right panels.

In these composite images, Fe XIV emission is found to be invariably linked to streamers, while Fe XI emission is found to be unequivocally associated with all open field lines throughout

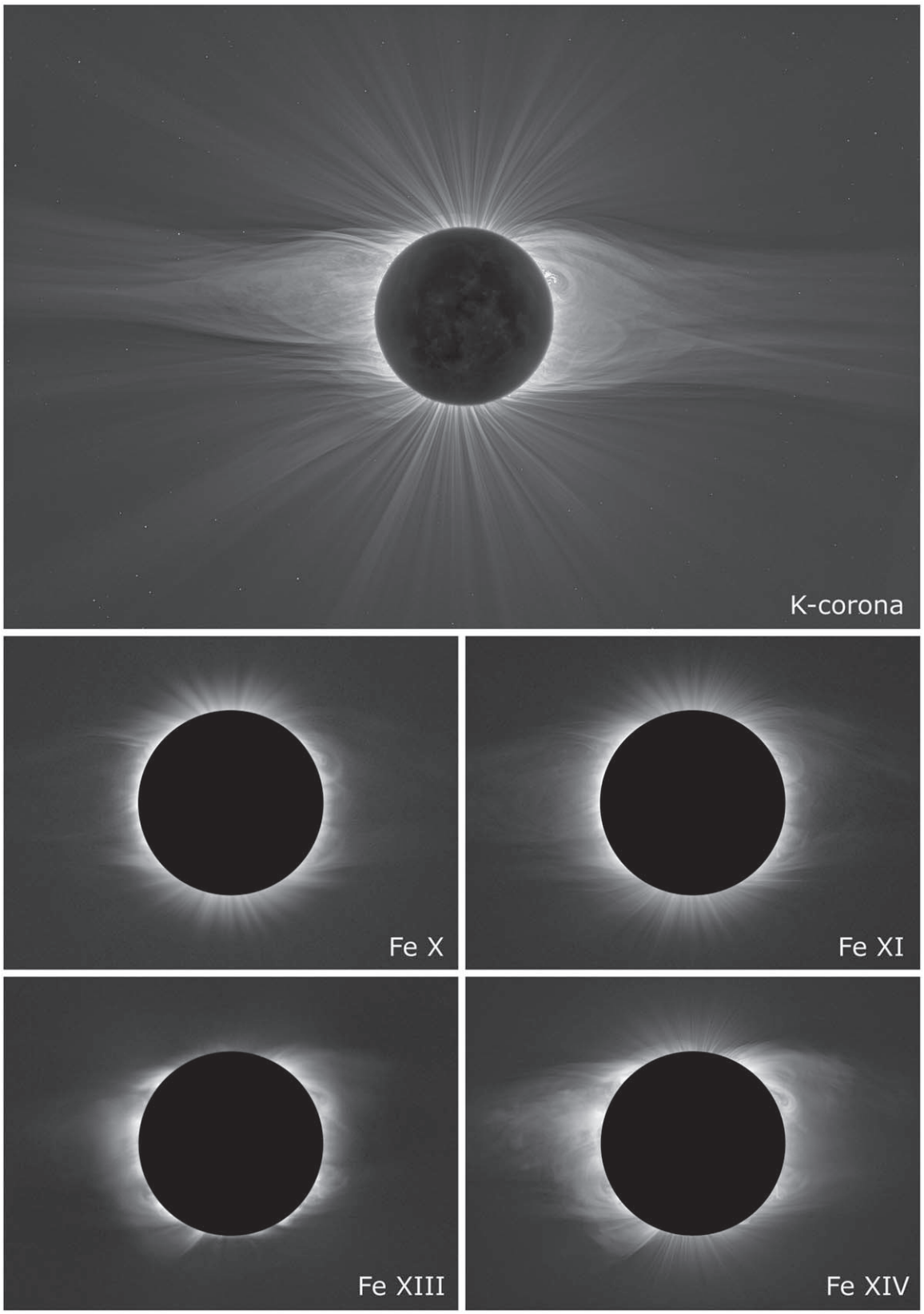

Figure 3. Comparison of white light, Fe X, Fe XI, Fe XIII, and Fe XIV emission from the 2019 total solar eclipse observations. Solar north is vertically up.

the corona. The latter also seems to often infiltrate streamers in the plane of the sky, underscoring the filamentary nature of all coronal structures and their low filling factor.

More importantly, the span of these observations over more than a full SC enables the investigation of the impact of solar activity not only on the topology of coronal magnetic fields but

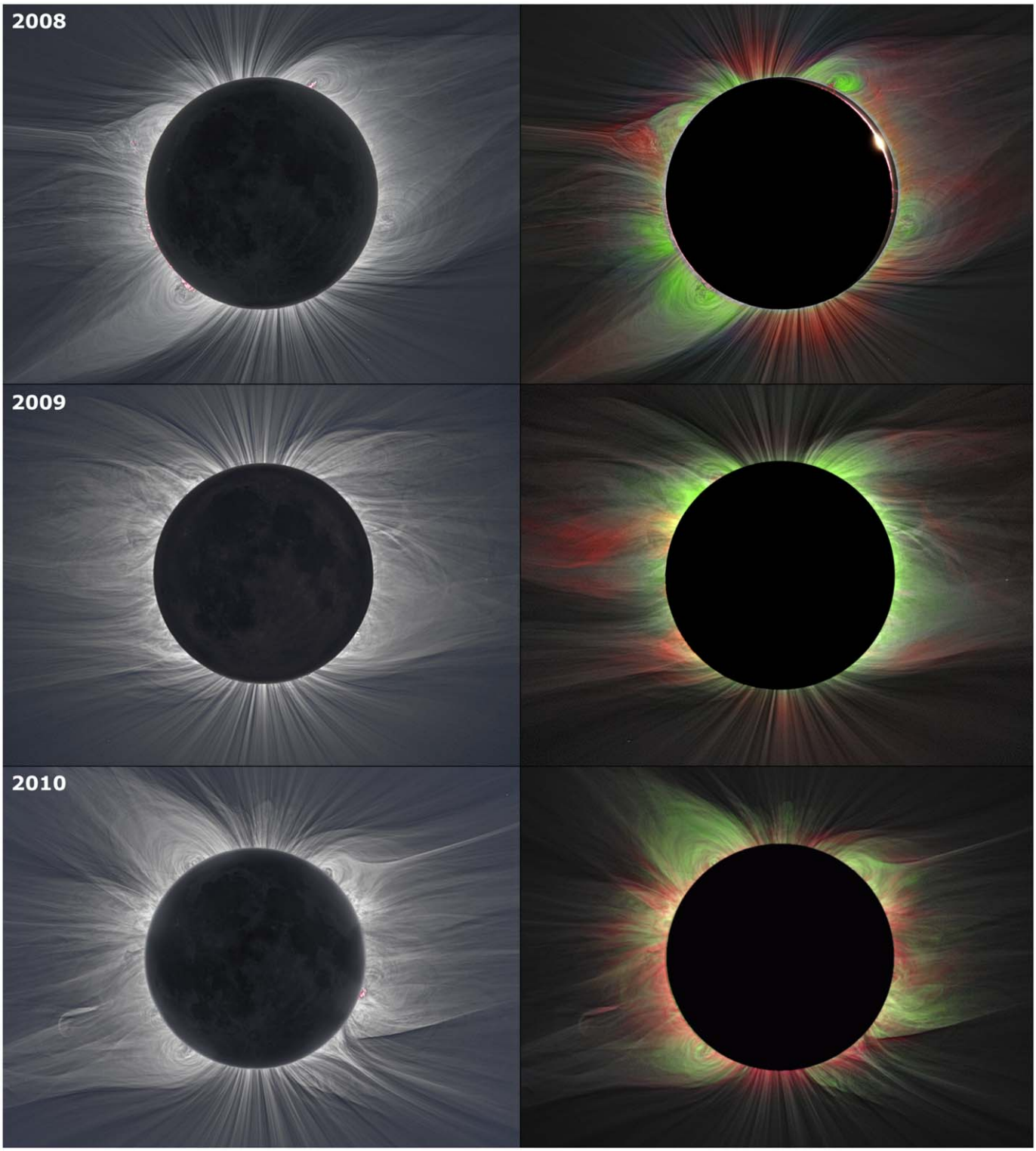

Figure 4. Composite from total solar eclipse images acquired between 2008 and 2010. To maximize the clarity of the images, they have been split into two panels. As in Figure 2(c), the white light image is given in the left column, and the overlay of white light with Fe XI 789.2 nm (red) and Fe XIV 530.3 nm (green) is in the right column. Solar north is approximately vertically up.

also on the temperature distribution in the corona. The temporal coverage from 2006 to 2020 shows that the spatial distribution of Fe XIV emission, characterized by $T_{\rm fexiv}$, changes across the corona as a function of time within a cycle. This change can lead to the unverified impression that the corona becomes hotter with increased solar activity. On the other hand, the ubiquity of the Fe XI emission persists regardless of solar activity, implying that the expanding corona is constrained to approximately $T_{\rm fexi}$ regardless of phase within an SC.

In summary, the spatial distribution and radial extent of the emission from Fe XI and Fe XIV in these composite images spanning more than an SC demonstrate, for the first time, how

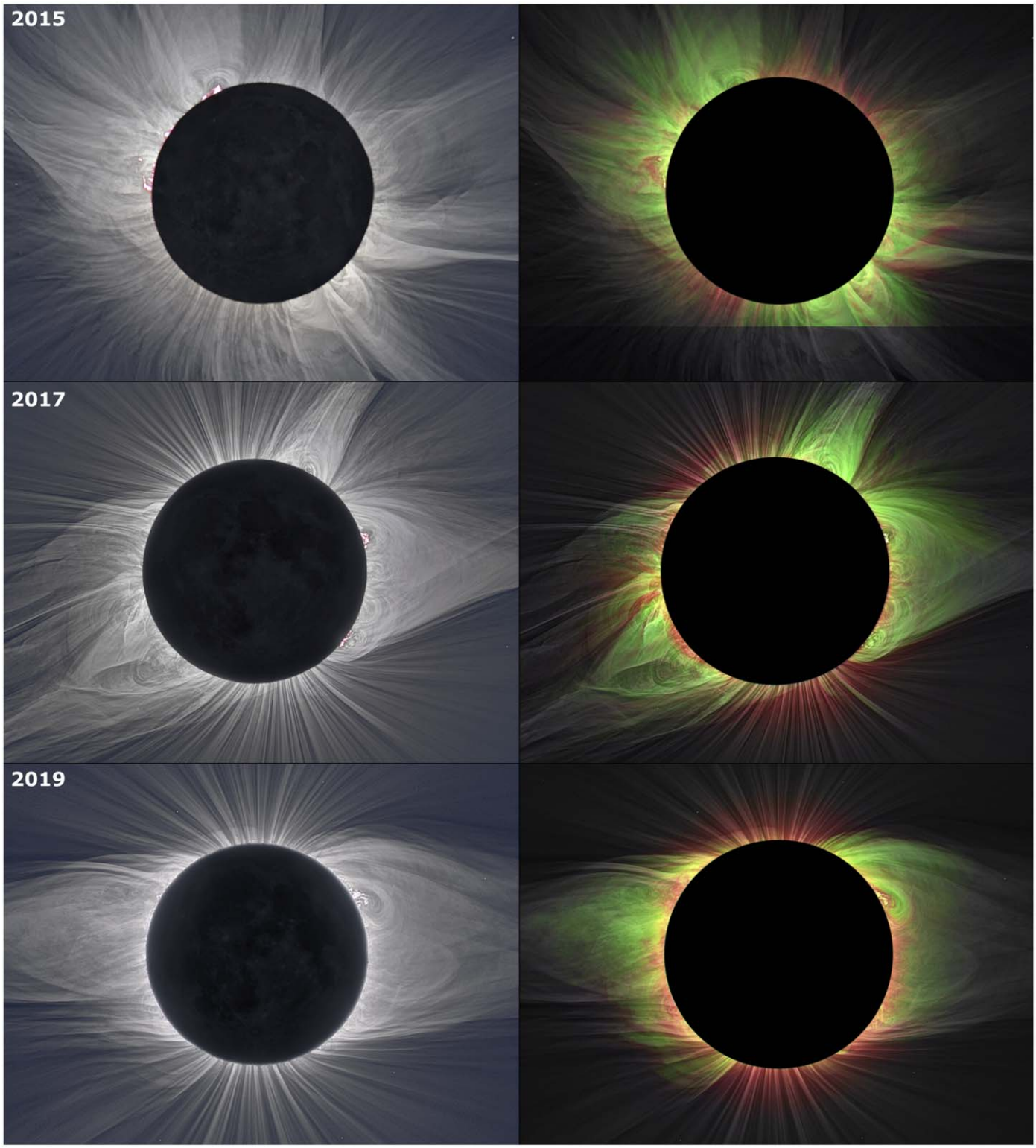

Figure 5. Same as Figure 4 for images acquired between 2015 and 2019. The gaps in emission line observations in 2012, 2013, and 2016 were due to poor observing conditions.

the distribution of the hotter Fe XIV coronal emission at $T_{\rm fexiv}$ changes throughout the different phases of an SC, while the cooler Fe XI emission at $T_{\rm fexi}$ remains spatially ubiquitous throughout the expanding corona, independent of phase within a cycle.

5. Manifestations and Sources of Dynamic Events in the Corona

Despite the very short duration of totality, eclipse images, whether in white light or coronal emission lines, capture not only the "static" state of the corona but also its instantaneous

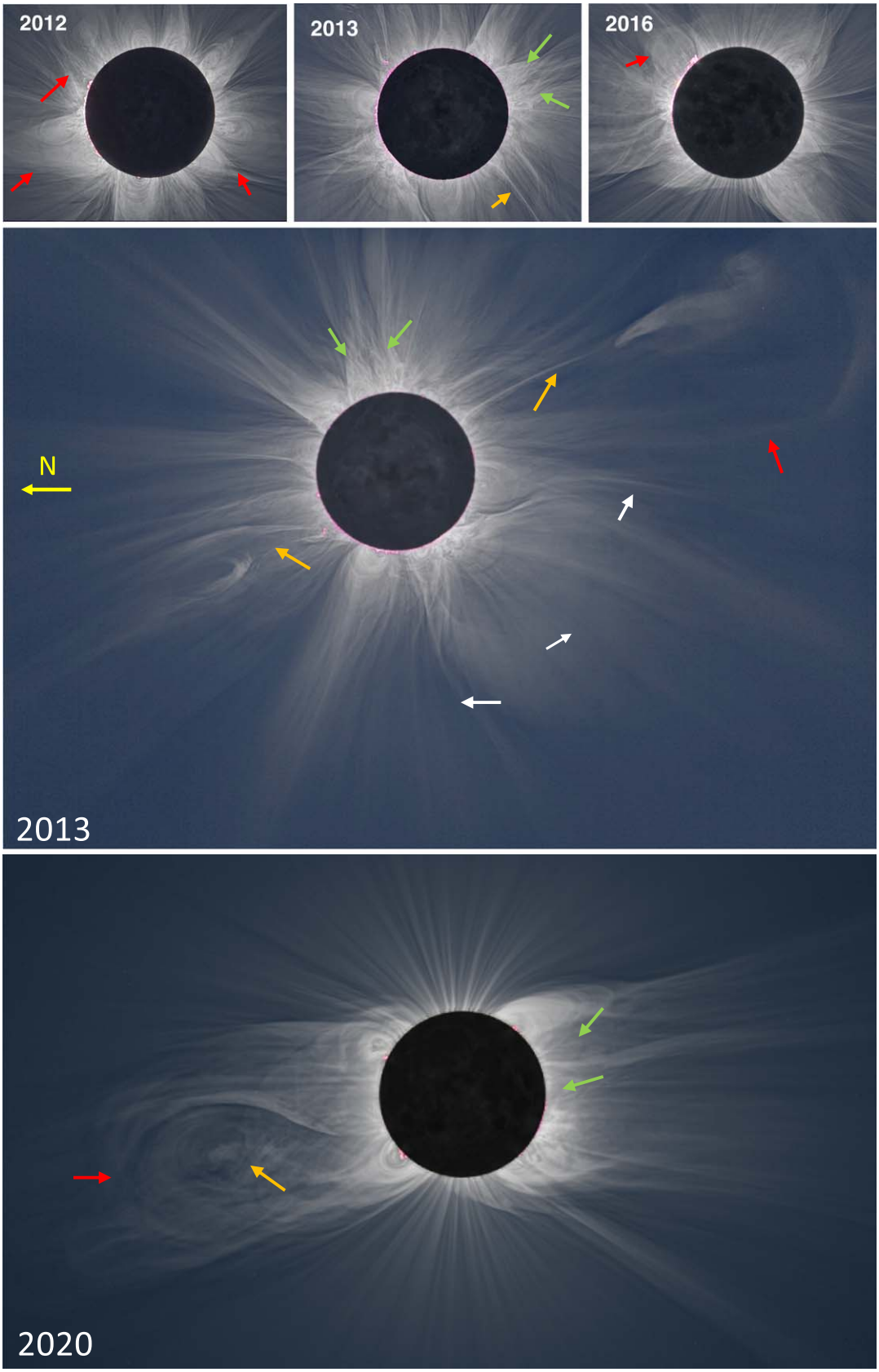

Figure 6. Top panels: white light images from 2012, 2013, and 2016. Middle panel: Larger field of view of the 2013 white light image showing the full extent of a bulblike CME envelope. Bottom: white light eclipse image from 2020 with a CME bubble. In all panels, red arrows point to CMEs, either at their emergence very close to the Sun, as in 2012 and 2016, or their full extent, as in 2013 and 2020. Green arrows point to wavy motions. Orange arrows point to prominence cores embedded within a CME. For 2013, the white arrows point to the bounding imprints of the passage of a CME. (Solar north is approximately vertically up in all panels except for the larger 2013 field of view, where it points to the left.)

dynamic status. Manifestations of dynamic events, such as CMEs, waves, and turbulence, are described next. It is shown how the distinct complex prominence structures are intricately connected to surrounding archlike structures and are the most likely drivers of the variable solar wind measured in situ.

5.1. CMEs, Waves, and Turbulence

Figure 6 is a compilation of the white light eclipse images from 2012, 2013, 2016 (top panels), and 2020 for which there were no corresponding coronal emission line images. This figure provides a comprehensive overview of dynamic structures, such as CMEs (red arrows), with their full extent captured in the wider fields of view of the 2013 and 2020 eclipses shown in the lower panels. In the 2013 wide field-of-view image, the faint boundary of the full CME bubble is shown by the red arrow. The prominence ejecta forming its core, as well as that of another CME almost diametrically opposite, are identified by the orange arrows. The two white arrows point to the imprint of a CME that had passed through the corona prior to the eclipse time (see Alzate et al. 2017 and Druckmüller et al. 2017, for more details). The green arrows point to wavy patterns. A full CME was also captured off the east limb in 2020 (red arrow), shown in the lower panel. The twisted features of the prominence ejecta (orange arrow) at its core are clearly evident. Wavy patterns (green arrows) are present off the west limb, as in 2013 and 2020.

Missing from these images is the temperature characteristic associated with the dynamic events. This information is, however, available in previous eclipses, such as those in 2017 and 2019 (see Figure 5). In 2017, the complex structure of the CME in the southeast was clearly dominated by Fe XIV emission, as found in streamers. In 2019, the bulge of the east streamer was dominated by large-scale eddies, also seen in Fe XIV emission.

5.2. Prominence–Corona Connectivity

It is clear from Figure 6 that prominences are intricately connected to dynamic events, as they expand within the core of CMEs while remaining tethered to the Sun. The examples in Figure 7 show that the link between prominences and the surrounding corona is far more ubiquitous. The 2013 example, shown in the top panel, is particularly informative. This eclipse was special because of its 40 s duration. As such, the angular extent of the Moon almost perfectly matched that of the solar disk, thus enabling coronal structures to be traced all the way down to the solar surface. This further enabled a perfect match with SDO/AIA He II 30.4 nm disk observations. The ubiquitous presence of prominences at the base of all streamers (indicated by the white arrows) is especially pronounced at solar maximum when streamers are almost evenly distributed around the solar limb.

Another fine example of the connectivity between prominences and surrounding coronal arches is shown in the details of the 2017 white light image in panels (b) and (c) in Figure 7, where the spatially resolved structures within two prominences were captured in two sections of the corona. The arrows point to the unmistakable connectivity between the filamentary structures belonging to a prominence and those associated with the overlying coronal arches mentioned earlier. The details in panel (d), taken from the 2008 eclipse, show how this connectivity reflects a link between the cool prominence material, typical of chromospheric emission, protruding into the corona and the hot Fe XIV emission in the bulge of

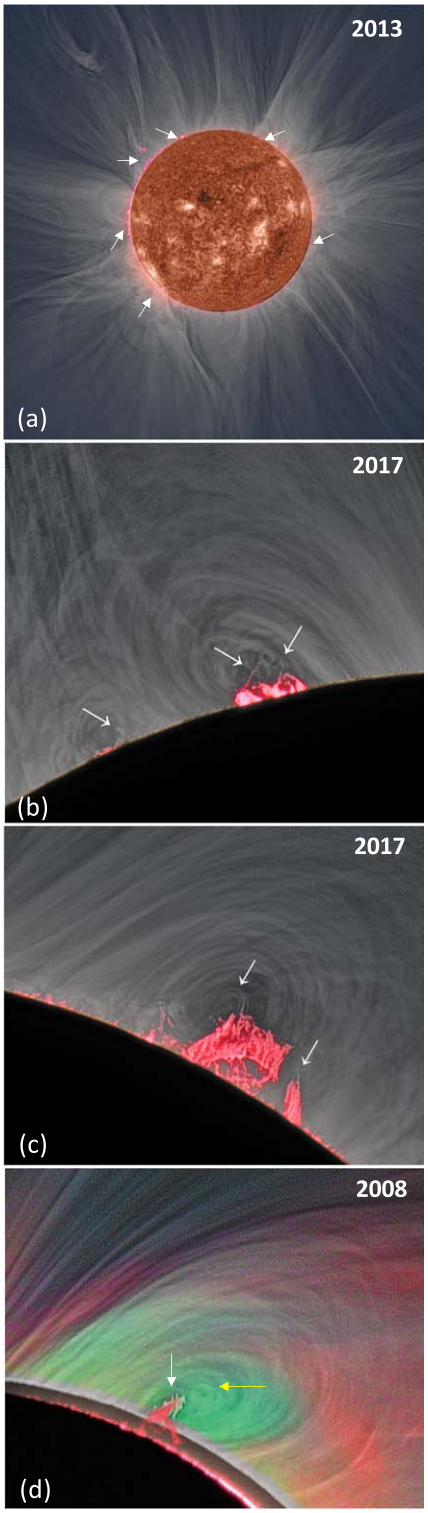

Figure 7. Connectivity between prominence structures (pinkish Hα emission) and large-scale coronal structures. (a) The 42 s 2013 eclipse was such that the Moon's angular extent was almost identical to the Sun's, thus enabling a perfect match between the SDO/AIA He II 304 chromospheric emission showing how all the prominences at the base of the corona around the solar disk are connected to the fine filamentary structures in the overlying corona. Panels (b) and (c) show two sections of the 2017 eclipse white light image. The arrows point to the links between filamentary structures in prominences and those in the overlying coronal structures. Panel (d) shows a prominence (white arrow) enshrouded by Fe XIV (green) emission (yellow arrow) taken during the 2008 eclipse. Red is Fe XI emission.

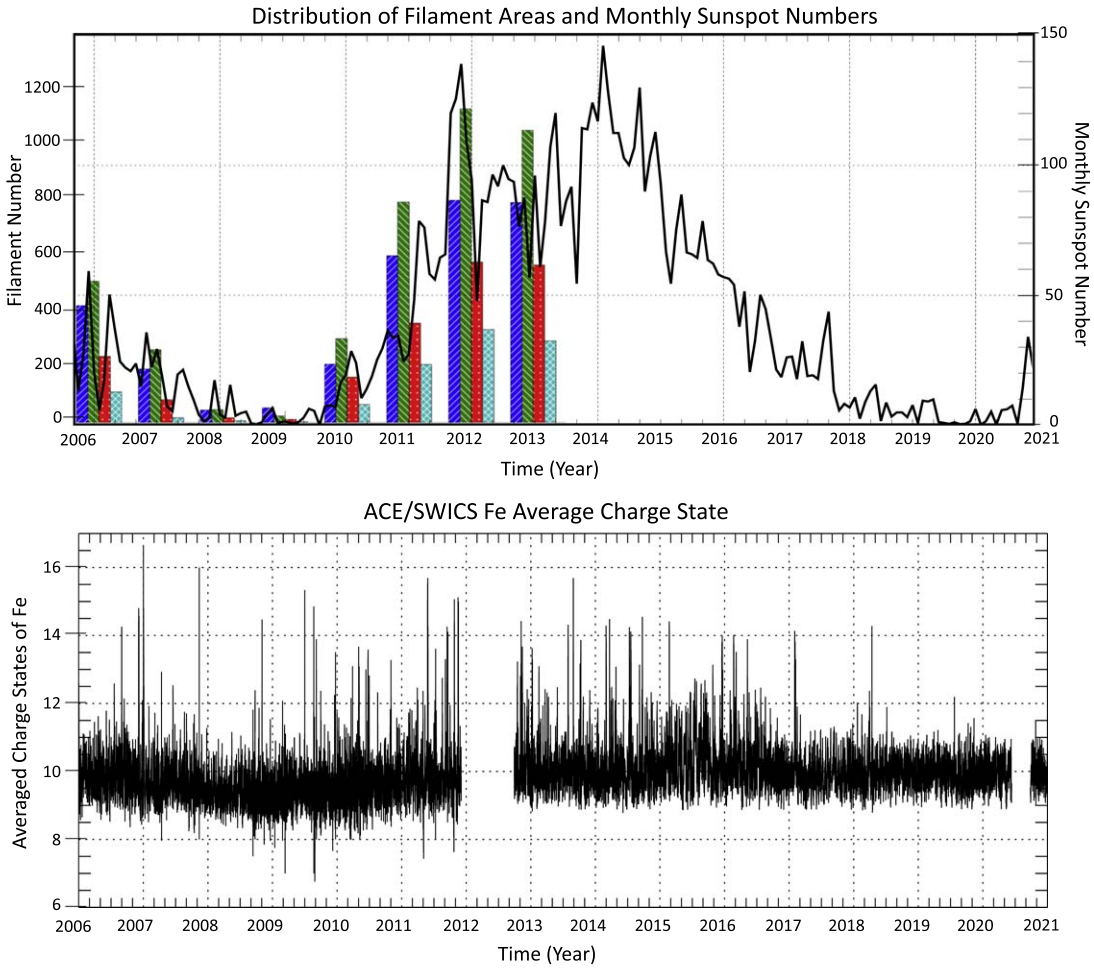

Figure 8. Top: overlay of monthly sunspot number and yearly histograms of the areal distribution of prominences on the solar surface up to 2013 (from Hao et al. 2015). The sunspot number extends to 2021 to cover the time span of the eclipse observations. In the histograms, dark blue is for areas $<2.5 \times 10^8$ km^2, green for the range 2.5×10^8–5×10^8 km^2, red for the range 5×10^8–1.0×10^9 km^2, and light blue for values $>1.0 \times 10^9$ km^2. Bottom: ACE/SWICS 12 minute averaged Fe charge states from 2006 to 2021, plotted every 2 hr.

streamers, referred to as "hot prominence shrouds" by Habbal et al. (2010c, 2014). This connectivity accounts for the close association of Fe XIV emission with CMEs, waves, and turbulence in the corona, as noted earlier.

5.3. Prominences and the Solar Cycle

The ubiquitous connectivity between prominences and streamers and the changes of the spatial distribution of the coronal temperature associated with changes in the spatial distribution of streamers as a function of SC strongly suggest that prominences play an essential role in driving the latter changes. Here we refer to the recent study by Hao et al. (2015) for additional supporting evidence. These authors explored the areal distribution of prominences across the solar surface using Hα data from Big Bear Solar Observatory collected over three cycles between 1988 and 2013. They binned their data into four categories depending on the areal coverage of prominences, as shown by the histograms in the top panel of Figure 8, together with a plot of the sunspot number covering the extent of the eclipse observations. (Unfortunately, the last data included in their study were from 2013.) A clear SC dependence is evident for all areal coverage bins.

The connectivity between prominences, surrounding coronal arches, and streamers established from the eclipse observations presented earlier, together with the change of the areal distribution of prominences across the solar surface as shown by Hao et al. (2015), provide further supporting evidence that prominences play a fundamental underlying role in triggering changes in the topology of the coronal magnetic field and thus changes in the spatial distribution of temperature in the corona with solar activity.

6. Connecting the Corona to the Solar Wind

Shown in the bottom panel of Figure 8 are the ACE Fe charge state measurements described earlier in Section 2.2, where they are referred to as the Fe average charge state, since they are the 12 minute averaged measurements plotted every 2 hr. They encompass the ions responsible for the Fe coronal emission lines, in particular Fe^{10+} for Fe XI and Fe^{13+} for Fe XIV. There are two noteworthy trends in this plot. (1) The Fe charge states are mostly clustered in a band between Fe^{9+} and Fe^{11+}, centered on Fe^{10+}, regardless of time within the SC, with a slight, yet statistically insignificant decrease in 2009. (2) The peaks in Fe charge states $>Fe^{11+}$ appear sporadically throughout the whole time period.

We next consider the solar wind speed data associated with the Fe average charge states. Given the large data volume, we choose two representative time periods: 2006 during the

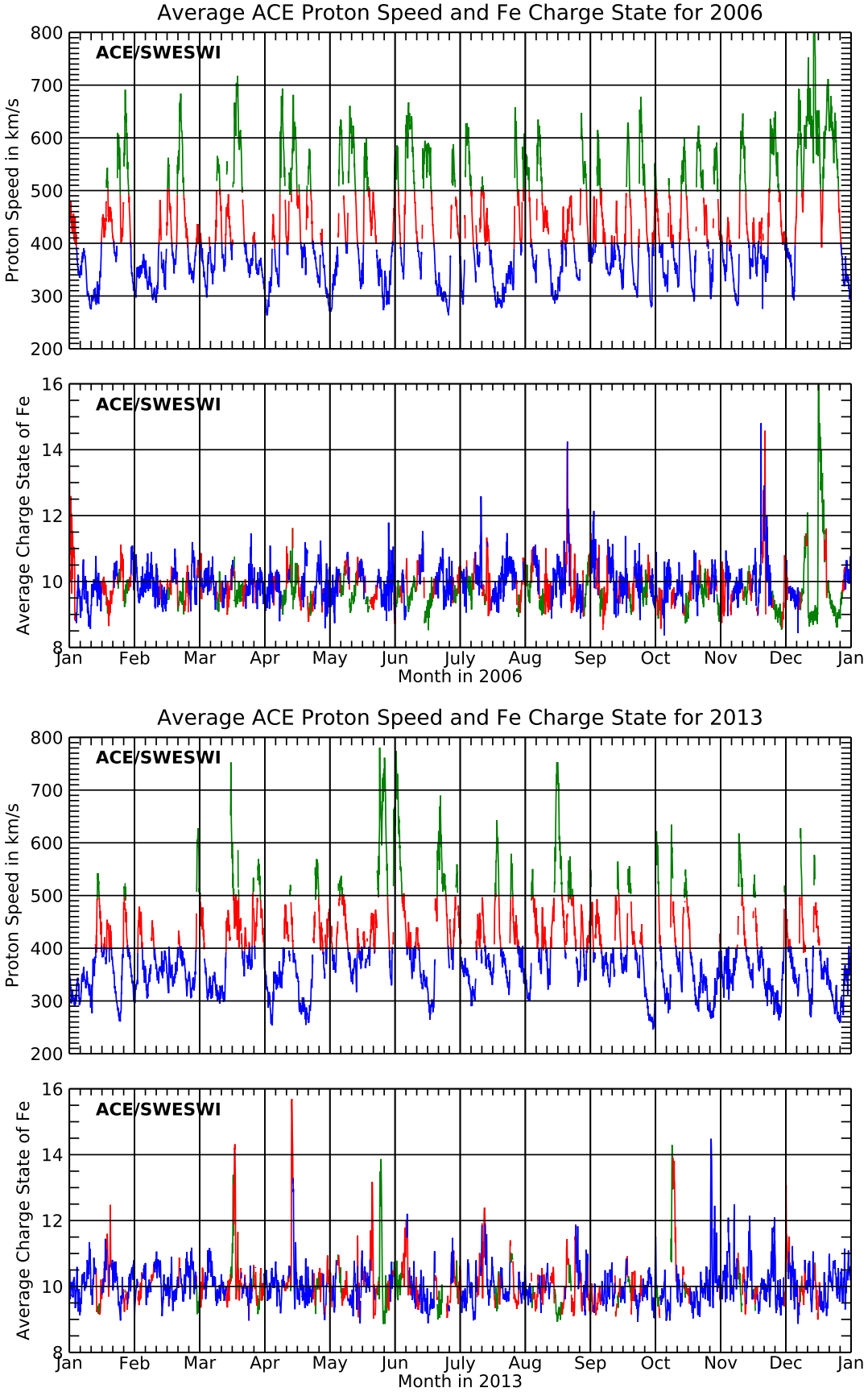

Figure 9. The 2 hr time-averaged Fe charge state and corresponding solar wind speed taken from the SWEPAM-SWICS data on ACE for 12 months in 2006 during the declining phase of SC 23 (top panels) and 2013 during the peak of SC 24 (bottom panels). Blue represents data for speeds below 400 km s^{-1}, red represents speeds in the range of 400–500 km s^{-1}, and green represents speeds greater than 500 km s^{-1}.

descending phase of SC23 and 2013 at solar maximum of SC24, as shown in Figure 9. The data have been color-coded for three speed ranges: blue for speeds $<400\,\mathrm{km\,s^{-1}}$, red for 400–500 $\mathrm{km\,s^{-1}}$, and green for speeds $>500\,\mathrm{km\,s^{-1}}$. The corresponding charge states are color-coded accordingly. It is clear from these data that solar wind streams vary continually in speeds between 300 and 700 $\mathrm{km\,s^{-1}}$ throughout the different phases of any given SC, despite the persistent prevalence of Fe^{10+}. These streams are thus referred to as the "continual" solar wind.

The freeze-in distance for Fe ions in the corona, inferred empirically by Boe et al. (2018) and from model calculations (e.g., Landi et al. 2012, 2014), shows that ionization equilibrium breaks down and ions become frozen in within the field of view of the eclipse observations. This implies that the in situ solar wind ion population, dominated by the Fe^{10+} ion charge state in situ, is already determined below a heliocentric distance range that is contained within observations of Fe XI emission in the corona. Furthermore, Figures 2(c), 4, and 5 consistently show the prevalence of Fe XI (Fe^{10+}) emission at any phase of the SC emission associated with plasmas at T_{fexi} throughout the corona. Thus, Fe^{10+} provides a fiducial link between the continual solar wind streams spanning speeds from 300 to 700 $\mathrm{km\,s^{-1}}$ and their T_{fexi} sources in the expanding corona, independent of SC activity.

The sporadic and occasional peaks in Fe charge states exceeding Fe^{11+} are most likely associated with ICMEs and CMEs in the corona. Inspection of the ACE ICME catalog (see Richardson & Cane 2010 and http://www.srl.caltech.edu/ACE/ASC/DATA/level3/icmetable2.htm) and the LASCO/C2 CME catalogs (https://cdaw.gsfc.nasa.gov/CME_list/) shows that in 2006, an interplanetary disturbance was identified at 14:14 UT on 14 December and 17:55 UT on 16 December (see top panels in Figure 9). Their most likely sources are a halo CME reported in LASCO C2 at 02:54 UT on 13 December with a linear speed of 360 $\mathrm{km\,s^{-1}}$, followed by a halo CME at 22:30 UT with a linear speed of 1042 $\mathrm{km\,s^{-1}}$ on 14 December. In 2013, an interplanetary disturbance with a speed of approximately 500 $\mathrm{km\,s^{-1}}$ identified in ACE at 22:54 UT on 13 April (see bottom panels in Figure 9) originated from a halo CME in the corona at 07:24 UT with a linear speed of 861 $\mathrm{km\,s^{-1}}$ on 11 April. While the association of CMEs with higher Fe charge states has been known for some time (e.g., Lepri et al. 2001), their drivers at the Sun had not been established.

Finally, we note that the other peaks in Fe charge states with relatively low speeds (red and blue) in Figure 9 have no corresponding references to CMEs in the aforementioned ACE and LASCO C2 catalogs. Those are most likely the result of dynamic events releasing hot material from streamers, since they are the only structures identified with the higher-temperature Fe XIV (Fe^{13+}) emission in the expanding corona. Given that prominences are the only dynamic entities identified in the eclipse images directly connected to streamers, they most likely enable the release of hot streamer material into the solar wind through sporadic magnetic reconnection.

7. Discussion

7.1. The Constancy of the Electron Temperature at the Source of the Continual Solar Wind

The composite eclipse images shown in Figures 2(c), 4, and 5 provide ample evidence of the manifestation of the different phases of an SC in the distribution of and changes in streamers. While evidence of the SC in the changing "shape" of the corona has been known from white light eclipse observations dating back to over a century (see, e.g., Hansky 1901; Mitchell 1932), the preponderance of topological open magnetic field structures originating at the solar surface and expanding out to several solar radii is far more pronounced in the high-resolution images presented here. The ubiquity of topologically open structures, also confirmed by the recent work of Boe et al. (2020b), who applied the rolling Hough transform to high spatial resolution white light eclipse images acquired between 2001 and 2019, underscores the view that sources of the expanding corona and the solar wind are not limited to polar coronal holes or the boundaries of streamers, as first pointed out by Woo & Habbal (1997 and Habbal & Woo (2001).

The direct association between Fe XI emission and open magnetic structures further underscores the constancy of the electron temperature at the source of the continual solar wind. The empirical inference of the electron temperature at the source of the solar wind has been a topic of continued investigation, given its role as an empirical constraint for models of solar wind acceleration. Earlier inferences from different instruments yielded a range of values (see, e.g., Habbal et al. 1993; David et al. 1998). One of the inherent limitations in inferences from remote-sensing observations is contamination from different temperature plasmas along the line of sight. Values quoted for coronal holes ranged from 0.7 to 1.6 MK, with a more likely average value below 1.3 MK, and 0.8–0.9 MK at their base (see Habbal et al. 1993). Recently, Morgan & Taroyan (2017) found that the mean coronal temperature from solar disk observations in the multifilter bandpasses of the SDO/AIA instrument spanning 2010–2017, which included the peak in SC 24, varied from 1.4 to 1.8 MK. However, the SDO/AIA observations have concerning limitations, since none of the designed spectral channels at 9.4, 13.1, 17.1, 19.3, 19.5, 30.4, and 35.5 nm contain emission from a single ion, thus impacting the reliability of the interpretation of the thermal characteristics of the coronal plasma, as recently noted by Del Zanna (2019).

However, inferences of average temperatures do not enable the distinction between the freely streaming coronal plasma, which we refer to as the "expanding" corona, and the coronal plasma bound to the Sun. By considering total solar eclipse images from coronal emission lines from distinct electron temperature plasmas straddling two SCs, an unequivocal identification of the temperatures associated with the two topologically different magnetic field structures dominating the corona was achieved.

There is no doubt that the solar wind evolves from its sources at the Sun into interplanetary space, as first comprehensively documented by the Helios measurements (Schwenn 1990). The evolution of the solar wind's characteristics with its expansion will continue to be a subject of exploration with NASA's Parker Solar Probe and ESA's Solar Orbiter. However, the unique set of total solar eclipse observations straddling more than a full SC, presented here, shows that the dominant presence of Fe^{10+} in topologically open coronal structures survives as the dominant ion in situ, regardless of the corresponding solar wind speed. This "continuous" link between the corona and the solar wind implies that the "continual" wind expanding from the corona reaches a range of speeds in interplanetary space, depending on

the physical parameters at their origin. Since the dominance of Fe XI emission in the expanding corona implies an almost constant $T_{\rm fexi}$ there, the density at the coronal base of solar wind streams thus becomes the main parameter that determines the asymptotic solar wind speed. This is indeed confirmed by earlier solar wind models by Leer & Holzer (1980) and Habbal et al. (1995). Simply stated, the energy input to higher-density wind sources at the Sun ends up being distributed among a larger number of particles, more so than for lower-density regions, thus leading to slower streams in the former and faster in the latter. Furthermore, the coronal conditions determining this continual wind imply that the same physical process in the corona drives the different speed streams. This yet-to-be-identified physical mechanism caps the electron temperature in the expanding corona at an almost constant value, $T_{\rm fexi}$, namely the peak ionization temperature of Fe^{10+}.

We caution that the $T_{\rm fexi}$ associated with Fe XI emission at the sources of the solar wind outflow, whether fast or slow, is probably uncertain to within ≈10%–20%, based on different published works (e.g., Del Zanna & DeLuca 2018; Landi, private communication). Indeed, the peak ionization temperatures presented in Figure 2 are subject to the assumption of ionization equilibrium, which is not necessarily valid in the corona. Regardless, the observations of Fe XI and Fe XIV emission in the corona indicate that the relative spatial distribution of the two charge states is the same observable seen in situ. Thus, even if the precise temperature values are not correct, the Fe XI and Fe XIV frozen-in charge states quantitatively link the solar wind types to their sources in the corona, as demonstrated here. In a sense, the temperature values are just a convenient number for understanding the observed charge ratio. The main result is that the constancy of $T_{\rm fexi}$ in the expanding corona, rather than its exact value, leads to the continual solar wind with a range of speeds.

7.2. Prominences, CMEs, and the Variable Solar Wind

These unique eclipse observations have demonstrated that prominences are ubiquitous at the base of streamers and are unmistakably connected to the overlying closed coronal structures forming the bulge of streamers, which are the hotter structures in the expanding corona (see Habbal et al. 2010c, 2014; Druckmüller et al. 2017). In fact, the most comprehensive extreme-UV space-based data from AIA/SDO lack the spatial extent and adequate temperature diagnostic to reach such a conclusion. Their limitation is particularly critical for understanding the thermal properties of CMEs, which originate within the bulges of streamers. It is through this link that the coolest material protruding into the corona, typical of chromospheric emission from neutral or low ionized atoms, finds itself enshrouded by the hotter coronal plasma (see Habbal et al. 2010c, 2014).

Prominences are known to be the most dynamic structures in the corona, with different types of instabilities developing at their coronal interface (see Druckmüller et al. 2014), and their frequent eruptions being directly linked to CMEs. As shown in Figures 6 and 7, the close link between the ejected prominence and coronal material forming a CME front is a direct consequence of the link between the two. The invariable association of ICMEs with high charge states in situ is further confirmation of this close link. Another signature of the consequence of prominence dynamics in in situ measurements is the detection of neutrals and low ionized atoms, characteristic of prominence plasmas (Gloeckler et al. 1998). Indeed, the fate of eruptive prominence material in conjunction with a CME was first reported by Ciaravella et al. (1997) in the UV and in a more comprehensive manner in the visible by Ding & Habbal (2017) during the 2015 total solar eclipse. The latter study captured Doppler redshifted emission in Fe XIV with speeds ranging from 100 to 1500 km s^{-1} associated about 10% of the time with emission from neutrals and low ionized atoms, characteristic of prominence material. These observations were the first to yield direct evidence for the escape of erupting prominence material, unscathed, into interplanetary space. Magnetic reconnection events within the prominence/corona interface remain an essential process for the release of the two extreme components, namely, neutrals and low ionized atomic states, and the highest charge states from bound structures in the corona. The variable solar wind, likely to also be turbulent, as visually present in the eclipse images, is then distinctly different from the continual solar wind. It is highly probable that the variable solar wind is associated with the sporadic presence of two extreme charge states: neutrals and/or low ionized charge states originating from ejected prominence material and charge states exceeding Fe^{13+} but not necessarily producing CMEs.

8. Conclusions

Images of the corona acquired simultaneously in white light, Fe XI, and Fe XIV during total solar eclipses between 2006 and 2020, thus spanning more than an entire SC, are presented here for the first time. Complemented by ACE in situ measurements of Fe charge states and solar proton speeds spanning the same time period, they yield novel insights into the coronal sources of the solar wind. Given that the Fe^{10+} and Fe^{13+} charge states, corresponding respectively to Fe XI and Fe XIV emission in the corona, are frozen in within the field of view of the eclipse images, their spatial distribution in the corona is then directly correlated with their corresponding charge state distribution in situ. In particular, this data complement points to the presence of continual solar wind streams dominated by Fe XI emission with a temperature $T_{\rm fexi} = 1.2 \pm 0.1$ MK in the expanding corona with in situ Fe charge states clustering around Fe^{10+} and speeds ranging from ≈300 to 700 km s^{-1} throughout the different phases of an SC. The spatial distribution of Fe XIV emission and Fe^{13+} charge states exhibits large variances with SC, indicating that the hotter corona and corresponding wind depend on large-scale coronal structures, notably streamers, changing with the SC.

This complement of coronal and in situ measurements also connects dynamic events in interplanetary space to the intrinsic dynamics of prominences, which are invariably linked to coronal arches forming the base of streamers, as well as active regions. Consequently, inevitable magnetic reconnection events within the complex structures of prominences and their surrounding regions lead to the expulsion of two extreme populations of plasma composition: neutrals and/or low ionized atoms and in situ Fe charge states exceeding Fe^{11+}. The high ionized charge states are linked to the confined high-temperature plasmas released from the bulges of streamers as a direct consequence of prominence dynamics, whether through the formation of CMEs or the release of a turbulent solar wind. The low charge states are remnants of expelled prominence material with typical chromospheric composition.

While the impact of the different phases of an SC is evident in the changing topology of streamers, it does not seem to have any effect on the unidentified physical processes that maintain the electron temperature at the sources of the continual outflow from the Sun at an almost constant value. These findings thus yield new constraints on models of the solar wind.

S.R.H. and the Solar Wind Sherpas acknowledge support from NASA and NSF for the eclipse observations spanning more than a solar cycle, the most recent grants being NASA grant NNX17AH69G and NSF grants AGS-1834662, AST-1733542, AST-1839436 to the University of Hawaii. N.A. acknowledges support from NASA through an appointment to the NASA Postdoctoral Program at the Goddard Space Flight Center, administered by the Universities Space Research Association under contract with NASA, and support under HGI grant No. 80NSSC20K1070. B.B. was supported by the National Science Foundation under award No. 2028173. M.D. was supported by the Grant Agency of Brno University of Technology, grant FSI-S14-2290. M.A.'s contribution to the eclipse observations was supported by Bridgewater State University CARS grants. We would also like to acknowledge valuable discussions with C. Haggerty, E. Landi, J. Scudder, and M. Velli, as well as the insightful input from the anonymous reviewer.

ORCID iDs

Shadia R. Habbal https://orcid.org/0000-0003-4089-9316
Miloslav Druckmüller https://orcid.org/0000-0001-7312-2410
Nathalia Alzate https://orcid.org/0000-0001-5207-9628
Adalbert Ding https://orcid.org/0000-0001-6573-7810
Benjamin Boe https://orcid.org/0000-0002-6396-8209
Sage Constantinou https://orcid.org/0000-0002-8937-5620
Martina Arndt https://orcid.org/0000-0002-7620-9738

References

Altrock, R. C. 2004, SoPh, 224, 255
Alzate, N., Habbal, S. R., Druckmüller, M., et al. 2017, ApJ, 848, 84
Badalyan, O. G., Obridko, V. N., & Sýkora, J. 2005, ARep, 49, 477
Boe, B., Habbal, S., Downs, C., & Druckmüller, M. 2021, ApJ, in press
Boe, B., Habbal, S., Druckmüller, M., et al. 2018, ApJ, 859, 155
Boe, B., Habbal, S., Druckmüller, M., et al. 2020a, ApJ, 888, 100
Boe, B., Habbal, S., & Druckmüller, M. 2020b, ApJ, 895, 123
Ciaravella, A., Raymond, J. C., Fineschi, S., et al. 1997, ApJL, 491, L59
David, C., Gabriel, A. H., Bely-Dubau, F., et al. 1998, A&A, 336, L90
Del Zanna, G. 2019, A&A, 624, A36
Del Zanna, G., & DeLuca, E. E. 2018, ApJ, 852, 52
Dere, K. P., Del Zanna, G., Young, P. R., et al. 2019, ApJS, 241, 22
Ding, A., & Habbal, S. R. , 2017, ApJL, 842, L7
Druckmüller, M. 2009, ApJ, 706, 1605
Druckmüller, M. 2013, ApJS, 207, 25
Druckmüller, M., Habbal, S. R., Alzate, N., et al. 2017, ApJL, 851, L41
Druckmüller, M., Habbal, S. R., & Morgan, H. 2014, ApJ, 785, 14
Druckmüller, M., Rušin, V., & Minarovjech, M. 2006, CoSka, 36, 131
Gloeckler, G., Cain, J., Ipavich, F. M., et al. 1998, SSRv, 86, 497
Habbal, S. R., Druckmüller, M., Morgan, H., et al. 2010a, ApJ, 708, 1650
Habbal, S. R., Druckmüller, M., Morgan, H., et al. 2010c, ApJ, 719, 1362
Habbal, S. R., Druckmüller, M., Morgan, H., et al. 2011, ApJ, 734, 120
Habbal, S. R., Esser, R., & Arndt, M. B. 1993, ApJ, 413, 435
Habbal, S. R., Esser, R., Guhathakurta, M., & Fisher, R. R. 1995, GeoRL, 22, 1465
Habbal, S. R., Morgan, H., Druckmüller, M., et al. 2010b, ApJL, 711, L75
Habbal, S. R., Morgan, H., Druckmüller, M., et al. 2013, SoPh, 285, 9
Habbal, S. R., Morgan, H., & Druckmüller, M. 2014, ApJ, 793, 119
Habbal, S. R., Morgan, H., Johnson, J., et al. 2007, ApJ, 663, 598
Habbal, S. R., & Woo, R. 2001, ApJL, 549, L253
Hansky, H. 1901, in the Total Solar Eclipse of May 1900, Report of the Expeditions Organized by the British Astronomical Association to Observe the Total Solar Eclipse of 1900 May 29, ed. E. W. Maunder (London: Knowledge Office), 89
Hao, Q., Fang, C., Cao, W., & Chen, P. F. 2015, ApJS, 221, 33
Landi, E., Gruesbeck, J. R., Lepri, S. T., et al. 2012, ApJ, 761, 48
Landi, E., Oran, R., Lepri, S. T., et al. 2014, ApJ, 790, 111
Leer, E., & Holzer, T. E. 1980, JGR, 85, 4681
Lepri, S. T., Zurbuchen, T. H., Fisk, L. A., et al. 2001, JGR, 106, 29231
McComas, D. J., Bame, S. J., Barker, P., et al. 1998, SSRv, 86, 563
Mitchell, S. A. 1932, ApJ, 75, 1
Morgan, H., & Taroyan, Y. 2017, SciA, 3, e1602056
Richardson, I. G., & Cane, H. V. 2010, SoPh, 264, 189
Rušin, V., & Rybansky, M. 2002, SoPh, 207, 47
Schwenn, R. 1990, in Physics of the Inner Heliosphere I, ed. R. Schwenn & E. Marsch (Berlin: Springer-Verlag), 99
Stakhiv, M., Lepri, S. T., Landi, E., Tracy, P., & Zurbuchen, T. J. 2016, ApJ, 829, 117
Stone, E. C., Frandsen, A. M., Mewaldt, R. A., et al. 1998, SSRv, 86, 1
Sýkora, J. 1992a, CoSka, 22, 55
Sýkora, J. 1992b, SoPh, 140, 379
Woo, R., & Habbal, S. R. 1997, GeoRL, 24, 1159